Solar RRL
www.solar-rrl.com

Sequential Deposition of Diluted Aqueous SnO_2 Dispersion for Perovskite Solar Cells

*Mikhail Pylnev, Ryosuke Nishikubo, Fumitaka Ishiwari, Atsushi Wakamiya, and Akinori Saeki**

The widespread use of tin dioxide (SnO_2) thin films as electron transport layer (ETL) of perovskite solar cells (PSCs) has been facilitated by commercial SnO_2 nanocolloid dispersion. Nevertheless, challenges such as nanoparticle agglomeration have emerged, impacting film quality and interface properties critical for PSC performance. Herein, the efficacy of sequential, multistep spin-coating of repeatedly diluted SnO_2 aqueous suspension as a simple and effective approach to enhance ETL properties is explored. Through systematic experiments using dynamic light scattering, cyclic voltammetry, optical spectroscopy, and photoconductivity, it is demonstrated that the sequential deposition significantly improves the flatness and coverage of SnO_2, leading to improved electron transport and transfer from a perovskite layer. Such a synergetic effect enables to fabricate lead iodide PSC ($FAPbI_3$, FA: formamidinium) with a power conversion efficiency of 22.99% compared to 20.48% for the conventional 1-step SnO_2 layer. The findings underscore the potential of sequential SnO_2 deposition as a promising technique for robust SnO_2 films of photoelectric conversion devices.

1. Introduction

Over the last 10 years, there has been remarkable progress in the advancement of organic–inorganic hybrid perovskite solar cells (PSCs), witnessing a remarkable gain in power conversion efficiency (PCE) from 3.8% to 26.1%.[1–6] The electron transport layer (ETL) plays a pivotal role in PSC devices, significantly influencing the overall efficiency of charge extraction in the device.[7] As such, SnO_2 thin films have emerged as popular choices for ETLs of PSCs owing to their high light stability and suitable energy level matching with perovskites.[8] Moreover, bulk electron mobility in SnO_2 can reach 250 $cm^2 V^{-1} s^{-1}$,[9–11] which is much higher than that in conventional TiO_2 (1 $cm^2 V^{-1} s^{-1}$).[10,12] Another advantage is the processing temperature for SnO_2 less than 200 °C[13] compared to ≈450 °C required for TiO_2 to obtain its anatase phase.[14,15] Furthermore, most of the recent PCE records for PSCs were achieved using SnO_2.[9,16,17] The commercially available SnO_2 nanocolloid dispersion further facilitates its widespread use as ETLs. However, subsequent studies revealed challenges such as SnO_2 nanoparticle agglomeration. Large SnO_2 agglomerates are formed spontaneously in the dispersion due to van der Waals interaction within SnO_2 nanoparticles, which have a large specific surface area in the dispersion.[18,19] This leads to poor contact with the substrate,[11,20] incomplete coverage by SnO_2 film,[18,21] stress and strain in the film and at the interface with perovskite layer,[19] and defects.[9,22,23] Moreover, the morphology of ETLs directly affects the subsequently deposited perovskite and other functional layers of PSCs.[20]

Several approaches were introduced recently to slow down the agglomeration of SnO_2 nanoparticles in the dispersion including doping with ethylenediaminetetraacetic acid (EDTA),[24] gadolinium acetate,[25] KCl,[26] ethoxylated polyethylenimine (PEIE),[27] NH_4Cl,[28] and NH_4F.[29] Moreover, the dopants passivate defects in the SnO_2 layers and allow to reduce the recombination rate at the interface with the perovskite layer. Thus, the open circuit voltage (V_{OC}) is increased. However, there are other approaches to improve SnO_2 films deposited from the dispersion including varying the pH level,[30] solvent engineering,[20] and introducing different bilayer combinations with SnO_2.[18,31–34] The main idea of these approaches is to improve the morphology of the ETLs and reduce the surface trap states.

M. Pylnev, R. Nishikubo, F. Ishiwari, A. Saeki
Department of Applied Chemistry
Graduate School of Engineering
Osaka University
2-1 Yamadaoka, Suita, Osaka 565-0871, Japan
E-mail: saeki@chem.eng.osaka-u.ac.jp

R. Nishikubo, F. Ishiwari, A. Saeki
Innovative Catalysis Science Division
Institute for Open and Transdisciplinary Research Initiatives (ICS-OTRI)
Osaka University
1-1 Yamadaoka, Suita, Osaka 565-0871, Japan

F. Ishiwari
PRESTO
Japan Science and Technology Agency (JST)
Kawaguchi, Saitama 332-0012, Japan

A. Wakamiya
Institute for Chemical Research
Kyoto University
Uji, Kyoto 611-0011, Japan

The ORCID identification number(s) for the author(s) of this article can be found under https://doi.org/10.1002/solr.202400415.

DOI: 10.1002/solr.202400415

In this study, we introduce a sequential deposition (SD) method for SnO_2, employing a diluted precursor suspension across multiple deposition steps to enhance control over film morphology and uniformity. This approach eliminates the need for additional chemicals, simplifying the fabrication process while ensuring rapid and efficient preparation. Systematic adjustment of precursor concentrations during deposition has significantly improved the quality of SnO_2 thin films, enhancing their adhesion and compatibility with perovskite layers. PSCs incorporating sequentially deposited SnO_2 demonstrate enhanced performance, achieving a maximum PCE of 22.99% with a higher V_{OC} of 1.106 V compared to control films (PCE of 20.48% and $V_{OC} = 1.057$ V). This method represents a promising pathway for achieving high-performance, low-temperature processed PSCs with improved stability and reproducibility.

2. Results and Discussion

The diagram illustrating SD is shown in **Figure 1**a. First, SnO_2 film was deposited from a precursor at a dilution of the aqueous SnO_2 dispersion at 1:3 (a volume ratio of as-received SnO_2 dispersion to water) (step 1) and then annealed on a hot plate at 120 °C for 30 min (step 2). This process is a typical procedure and defined as a control in this study. Then, the SnO_2 aqueous dispersion was diluted with water to the same vial (step 3), deposited on the top of the previous SnO_2 film (step 4), and annealed again at the same condition (step 5). Steps 3–5 were repeated sequentially, as listed in **Table 1**.

Figure 1b depicts the dynamic light scattering (DLS) histogram of a commercial SnO_2 aqueous colloidal dispersion (initially at 15 wt% in H_2O) diluted with water at different ratios. It is evident that as the concentration decreases, the distribution of the SnO_2 particles becomes more uniform, and the aggregate size decreases. Figure 1c shows the average particle size and full-width at the half maximum (FWHM) of the histogram of the diluted suspensions. A significant and continuous reduction in the average particle size was observed from 310 nm of the frequently employed 1:3 (v:v) dilution (control)[35–43] to 200 nm of 1:15. Beyond 1:15, the average particle size shows a plateau. The observed shift is due to the reduction of excessive nanoparticle aggregation and improved dispersion. Additionally, dilution facilitates more effective penetration of stabilizing agents throughout the dispersion, leading to improved uniformity and stability. The FWHM values linked to the uniformity of the particle distribution decrease sharply from 330 nm for 1:3 dilution to 127 nm for 1:10 dilution, whereas upon further dilution fluctuate around this value. Since the DLS analysis revealed that the change in distribution saturated at the ratio of 1:15, this value was chosen as a starting point for further evaluation.

Figure 2a displays atomic force microscopy (AFM) images of SnO_2 layers on fluorine-doped tin oxide (FTO) prepared according to control, SD-1, and SD-3 methods. The SD-1 and SD-3

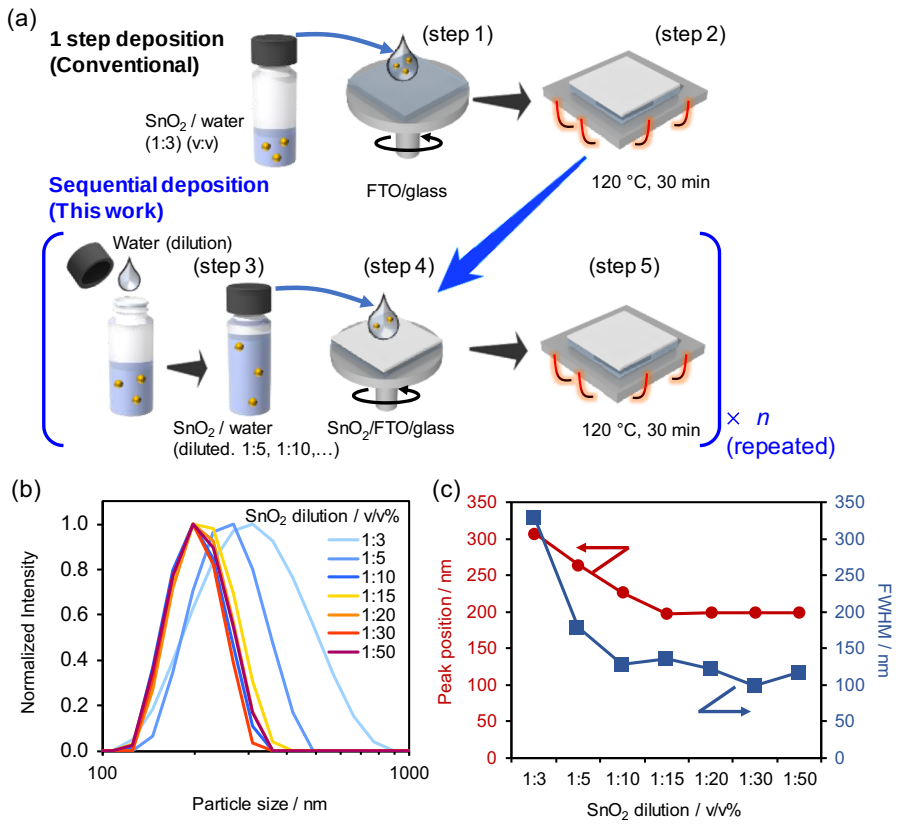

Figure 1. a) Diagram illustrating SD. b) Particle size histograms obtained from the DLS analysis for diluted SnO_2 colloidal aqueous suspensions with water at ratios of 1:3, 1:5, 1:10, 1:15, 1:20, 1:30, and 1:50 (v:v). c) Peak position and FWHM values of (b).

Table 1. Details of the preparation of SD of SnO_2[a].

Dilution[b]	1:3	1:15	1:20	1:20	1:30	Total step	SFE [mJ m^{-2}][d]	J_{cp} [μA cm^{-2}][e]	ΔE_p [V][f]	Thickness SEM [nm]	Thickness AFM [nm]
Rotation [rpm][c]	3000	3000	3000	5000	7000						
FTO	–	–	–	–	–	–	46.4	150.8	0.078	–	–
Control	V	–	–	–	–	1	53.1	68.9	0.555	77.7 ± 26.3	63.3 ± 10.4
SD-1	V	V V	–	–	–	3	60.5	50.6	0.752	69.6 ± 11.2	58.2 ± 9.7
SD-2	V	V V	V V	–	–	5	62.2	47.7	0.824	–	–
SD-3	V	V V	–	V V	–	5	64.0	46.0	0.829	61.2 ± 8.8	44.6 ± 9.3
SD-4	V	V V	V V	–	V V	7	67.3	40.4	0.841	–	–
SD-5	V	V	–	V	V	4	63.4	47.8	0.816	–	–

[a]One deposition process is indicated by "V". "V V" means deposition done twice. [b]Dilution of as-received SnO_2 suspension relative to water in v:v%. [c]Rotation per minute (rpm) of spin coating for 30 s. For each step, the film was annealed at 120 °C for 30 min. [d]SFE. [e]Cathodic peak current density of CV. [f]Peak-to-peak separation of CV.

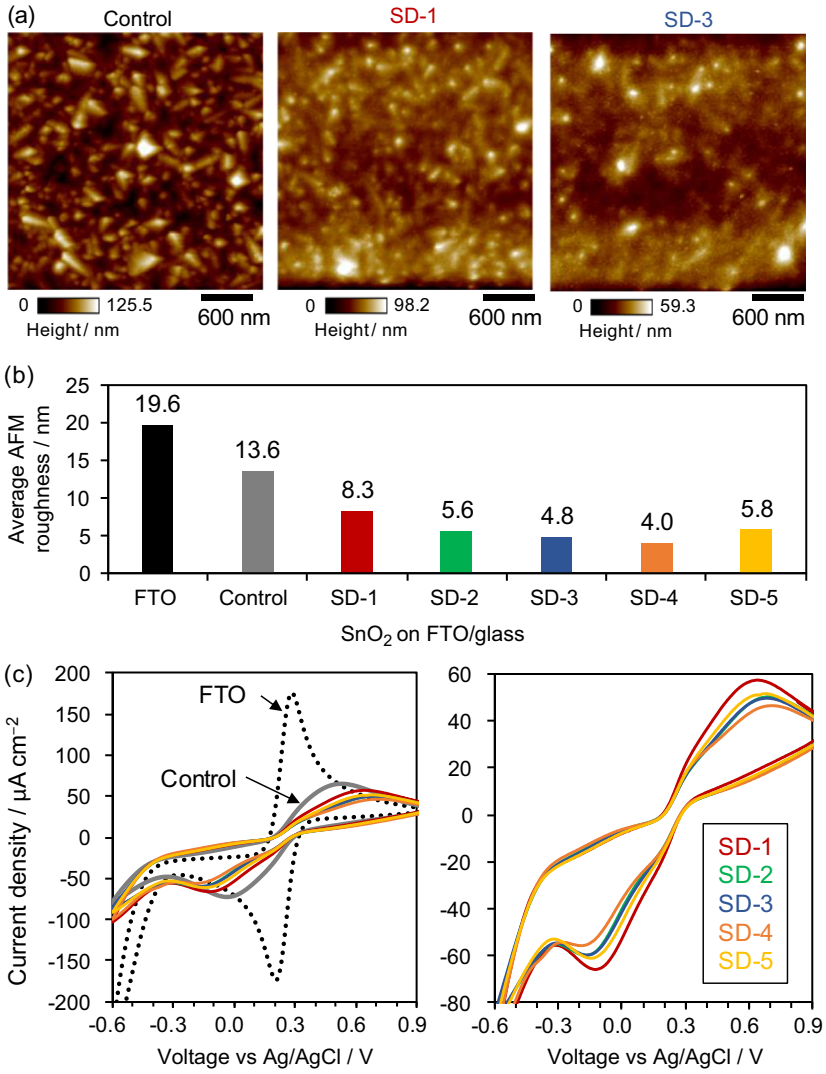

Figure 2. a) AFM height images of SnO_2 layers prepared via a standard route (control, dilution of SnO_2 aqueous dispersion 1:3 (v:v)) and via SD methods (SD-1 and SD-3). The color range of control, SD-1, and SD-3 are 125.5, 98.2, and 59.3 nm, respectively. b) Histogram of the average AFM roughness for different samples. c) Left panel: CV of FTO, SnO_2 films prepared via the control and SD (SD-1 to SD-5). Right panel: zoomed curves. Those of FTO and control are not shown.

processes correspond to 3 layers (diluted suspensions of 1:3 and double 1:15) and 5 layers (those of 1:3, double 1:15, and double 1:20) depositions. The details of these methods are listed in Table 1, and all AFM images of SnO_2 prepared by other methods (control, and SD-1 to SD-5 including a bare FTO substrate) are provided in Figure S1, Supporting Information. The average AFM roughness (R_a) of the samples was measured and is shown in Figure 2b. The roughness (originally 19.6 nm for bare FTO) decreases from 13.6 nm for control SnO_2 to 8.3 nm for SD-1 SnO_2 and to 4.0 nm for SD-4 SnO_2. SnO_2 possesses exceptional chemical stability, ensuring that once a film forms, it remains firmly in place without the risk of being washed away by the subsequent depositions from aqueous solutions. From the AFM measurements, we conclude that layer-by-layer deposition of SnO_2 holds promise for preparing a smooth film.

Figure 2c presents cyclic voltammograms (CV) of the films prepared by the control and SD methods. The cathodic peak current density (J_{cp}) serves as an indicator for the amount of current flow and hole-blocking ability. Meanwhile, the peak-to-peak separation between the cathodic and anodic peak potentials (ΔE_p) indicates charge transfer resistance (a larger ΔE_p suggests a better film coverage; Figure S2, Supporting Information).[44] Across all SnO_2 deposited samples, the redox reaction is subdued, as evidenced by the decrease in $J_{cp} < 70\ \mu A\ cm^{-2}$ and increase in $\Delta E_p > 0.5$ V compared to that of bare FTO ($J_{cp} = 150.8\ \mu A\ cm^{-2}$ and $\Delta E_p = 0.078$, Table 1). This means all SnO_2 films successfully cover the FTO substrate. Notably, the J_{cp} and ΔE_p values for the sequentially deposited films ($< 50\ \mu A\ cm^{-2}$) are lower than that of the control SnO_2 film ($68.9\ \mu A\ cm^{-2}$), while ΔE_p reaches 0.8 V compared to 0.55 V for the control film. These indicate that SD effectively improves the coverage and uniformity of the films.

To determine the ideal number of sequential layers and other deposition parameters, we also measured contact angles with water and glycerol (Figure S3, Supporting Information). The surface free energy (SFE) was calculated based on the Kaelble–Uy theory (Table 1 and Table S1, Supporting Information).[45] There are a few observations from SFE, J_{cp}, and AFM roughness: 1) SDs with further dilution should be done at increasing rotation per minute (rpm) during spin-coating. When comparing SD-2 (3000 rpm) and SD-3 (5000 rpm), the average AFM roughness (5.6 vs 4.8 nm) decreased by just increasing the rpm of deposition. This could be due to increased spreading and thinning of the sol during faster spinning, leading to less irregularities on the surface. However, the SFE, J_{cp}, and ΔE_p did not change much with increasing the rpm, indicating that further dilution is required; and 2) A double SD from the same diluted dispersion is better than a single deposition from gradually diluting dispersions. The SD-3 film consisting of five layers (once 1:3, twice 1:15, and twice 1:20 diluted suspensions) showed improved J_{cp} of $46.0\ \mu A\ cm^{-2}$ compared to $47.8\ \mu A\ cm^{-2}$ for the SD-5 film consisting of four layers prepared from successively diluted suspensions (once for 1:3, 1:15, 1:20, and 1:30 diluted suspensions). Moreover, there is a more significant decrease in average AFM roughness of SD-3 (4.8 nm) than SD-5 (5.8 nm). Overall, it is easier and more beneficial to deposit the diluted dispersion twice instead of diluting it at each step of dilution. Overall, two methods of sequential SnO_2 deposition were chosen and studied further, namely, conditions of SD-1 and SD-3.

To provide a thorough examination of the morphology of sequentially deposited SnO_2 films, scanning electron microscope (SEM) images were captured and are presented in **Figure 3**a–d. The control SnO_2 film (Figure 3b) reveals a coarse-grained structure with sizable gaps between the grains and still resembles the

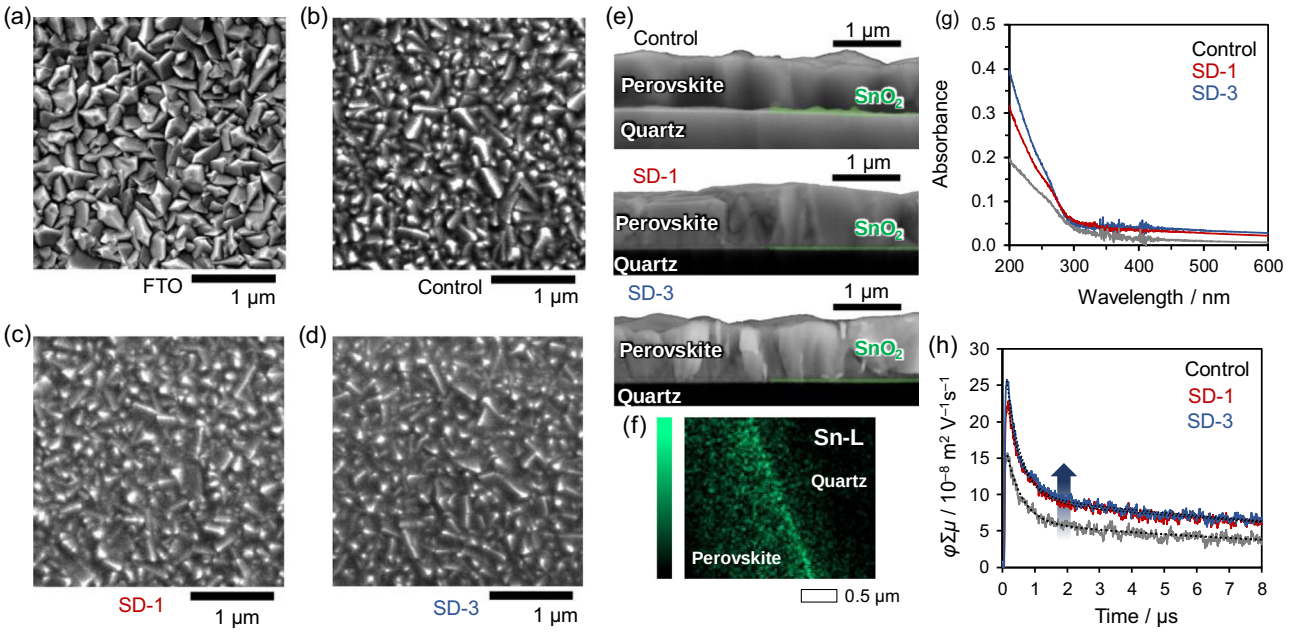

Figure 3. a) SEM images of FTO, b) control SnO_2 on FTO, c) SD-1 SnO_2 on FTO, and d) SD-3 SnO_2 on FTO. e) Cross-sectional SEM images of $FAPbI_3$ on SnO_2/quartz (top: control, middle: SD-1, bottom: SD-3). The SnO_2 layer is drawn in green color at the half left part. The scale bars in a–e) are 1 μm. f) Sn-L EDX map of the cross-sectional image of $FAPbI_3$ on SD-3 SnO_2. g) UV–vis absorption spectra of SnO_2 on quartz. h) TRMC decays (the dashed lines are double-exponential fitting curves) of SnO_2 on quartz ($\lambda_{ex} = 266$ nm).

morphology of bare FTO (Figure 3a). This is indicative of incomplete coverage and potential aggregation of particles during deposition. In contrast, the sequentially deposited SnO_2 films (SD-1 and SD-3) display a distinctively smooth appearance without evident pinholes (Figure 3c and d, respectively). This observation aligns with the findings from CV analysis, where the anodic current and peak-to-peak separation are notably improved for sequentially deposited films. This improvement in surface morphology suggests the efficacy of SD in promoting film homogeneity and coverage.

Figure 3e shows cross-sectional SEM images of the $FAPbI_3$ perovskite (FA: formamidinium, the surface SEM images are discussed later) on SnO_2/quartz. The magnified images are provided in Figure S4, Supporting Information. The thickness of the perovskite layer was mostly the same of ≈600 nm. In contrast, the thicknesses of SnO_2 layer were decreased from 77.7 ± 26.3, 69.6 ± 11.2, to 61.2 ± 8.8 nm for control, SD-1, and SD-3 SnO_2, respectively (Table 1). Interestingly, the thickness decreases with subsequent depositions, suggesting that each deposition of the diluted SnO_2 aqueous precursor results in partial dissolution of the underlying layer. This observation contradicts the conventional understanding that, after annealing, the SnO_2 layer should remain stable without significant dissolution, and that each additional spin-coating generally contributes to an increase in the film thickness. Thus, the thickness of the layers was measured by AFM (Figure S5, Supporting Information). The results are 63.3 ± 10.4, 58.2 ± 9.7, and 44.6 ± 9.3 nm for control, SD-1, and SD-3 SnO_2, respectively (Table 1), and the trend is consistent with the SEM observations. To further understand the reason for the decreased thickness, we performed X-Ray photoelectron spectroscopy (XPS) measurements on the samples (Figure S6, Supporting Information). The Sn 3*d* peaks of SD-1 and SD-3 samples shifted toward the lower energy by 0.15 and 0.29 eV, respectively, compared to the control sample. Similarly, the O 1*s* peaks (Sn-O, OH, and H_2O) of the SD samples were negatively shifted by 0.22 and 0.33 eV, respectively. As listed in Table S2, Supporting Information, the $O_{Sn\text{-}O}/O_{O\text{-}H}$ ratio increases from 1.07 for the control sample to 1.19 and 1.41 for SD-1, and SD-3 SnO_2 samples, respectively. Moreover, the $O_{Sn\text{-}O}/O_{H_2O}$ ratio is almost doubled for the SD samples. The shift of the XPS peaks to the lower energy implies a more negatively charged chemical environment.[46] Since the shift is increasing with each sequentially deposited layer (from SD-1 to SD-3), as well as the amount of OH^- groups and water on the surface, we claim that SD leads to partial hydroxylation and hydration of the SnO_2 layers underneath. This can explain a slight decrease in the thickness, as well as an increase in the flatness of the SnO_2 layer with each additional deposition from the diluted solutions.

Another notable observation is that the mean absolute error of thickness measured by SEM, indicative of layer uniformity, decreases from ±26.3 nm for the control to ±11.2 and ±8.8 nm for the SD process. This aligns well with the AFM surface measurements, where the average roughness decreased significantly from 13.6 nm for the control SnO_2 to 4.8 nm for the SD-3 SnO_2. Figure 3f shows an energy-dispersive X-Ray (EDX) Sn-L map of a cross-sectional image of SD-3 SnO_2. The map confirms that the presence of SnO_2 between the perovskite layer and the quartz substrate. The reflection mode SEM image and other elemental EDX images (Pb and O) are provided in Figure S7, Supporting Information.

Figure 3g shows the ultraviolet–visible (UV–vis) absorption spectra of control, SD-1, and SD-3 SnO_2 films. Interestingly, the absorbance increases with each additional deposition step, despite their reduced thicknesses. Accordingly, this signifies a denser packing of material or alterations in its optical properties, resulting in heightened light absorption. The Urbach energy derived from the high-energy regions (4–5 eV) is 0.64 eV for the control SnO_2 and drops to 0.59 for SD-1 and even further to 0.50 eV for SD-3 (Figure S8, Supporting Information). Lower Urbach energy values indicate a reduction in disorder and/or defects and support the improved structural quality of the sequentially deposited SnO_2 films. The optical bandgap energy (E_g) of SnO_2 estimated from the Tauc plots were 4.24, 4.26, and 4.35 eV for control, SD-1, and SD-3, respectively (Figure S9, Supporting Information), which was larger than the reported E_g of ≈3.7 eV for a powdered SnO_2 sample.[47] This discrepancy can be attributed to the thinness of the SnO_2 films. Subsequently, we evaluated an E_g of a drop-casted SnO_2 film and found it to be ≈3.9 eV. The X-Ray diffraction (XRD) patterns of these spin-coated and drop-casted films reveal only an amorphous quartz background (Figure S10, Supporting Information). No detectable peak is possibly due to the small thickness and/or the small crystallite size.

Figure 3h displays the flash-photolysis time-resolved microwave conductivity (TRMC)[48] transients of SnO_2 on quartz. The decays analyzed by double exponential functions exhibit no distinct change in the average lifetime (τ_{ave}) among the control, SD-1, and SD-3 samples (Table S3, Supporting Information). However, the $\varphi\Sigma\mu$ maxima ($\varphi\Sigma\mu_{max}$, φ: the charge carrier generation yield and $\Sigma\mu$: the sum of the hole and electron local mobilities) show a continuous increase from $1.5 \times 10^{-7}\,m^2\,V^{-1}\,s^{-1}$ for the control to $2.3 \times 10^{-7}\,m^2\,V^{-1}\,s^{-1}$ for SD-1 and $2.6 \times 10^{-7}\,m^2\,V^{-1}\,s^{-1}$ for SD-3. This increase mostly in mobility ($\Sigma\mu$) may stem from decreased defect density on the surface along with the improved morphology. This aligns well with the results of SFE analysis and SEM observation. Note that φ remains approximately the same across the samples, as the excitation photon energy ($\lambda_{ex} = 266$ nm equivalent to 4.66 eV) is much larger than the E_g of SnO_2.

To scrutinize the effect of SD on the performance of PSCs, $FAPbI_3$ layers were deposited on SnO_2 prepared by the control and SD methods (SD-1 and SD-3). As shown in **Figure 4**a, the SEM images of the perovskite layers display almost similar morphology, where the averaged grain sizes are 1.11 μm for the control, 1.16 μm for SD-1, and 1.17 μm for SD-3 samples (Figure S11, Supporting Information). The XRD patterns (Figure 4b) of the perovskite layers deposited on different SnO_2 layers show no big difference. All films reveal pure α-$FAPbI_3$ with a peak at $2\theta_1 = 14.3°$ and an insignificant amount of PbI_2 phase at $2\theta_2 = 12.0°$. The ratio of the intensities at these peaks ($I_{\theta_1}/I_{\theta_2}$) is 25–30 for all samples, indicating a minor effect of the passivation and/or blocking by remnant PbI_2.

The UV–vis photoabsorption spectra of the perovskites were not so affected; however, the photoluminescence (PL) intensities increased steeply from the control to SD-1 (1.40 fold) and SD-3

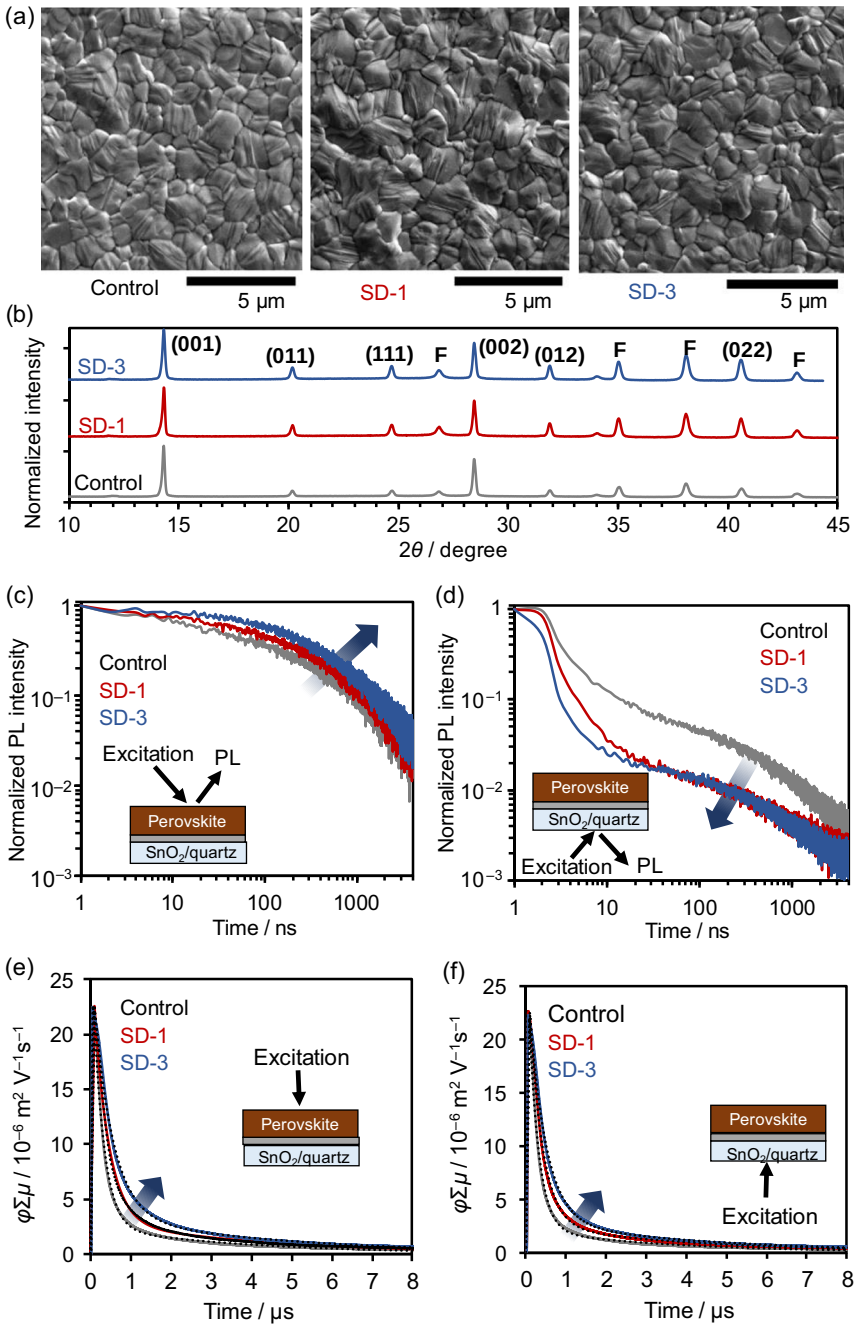

Figure 4. a) SEM images of $FAPbI_3$ on SnO_2/FTO prepared by the control, SD-1, and SD-3 methods. b) XRD patterns of the perovskite on control, SD-1, and SD-3 SnO_2 on quartz; the peaks belonging to α-$FAPbI_3$ are labeled with their respective Miller indices in parentheses, F indicates FTO peaks. TRPL decays of the $FAPbI_3$ on control, SD-1, and SD-3 SnO_2 on quartz excited from c) perovskite side and d) quartz side. $\lambda_{ex} = 377$ nm and $\lambda_{em} = 800$ nm. TRMC decays of perovskite on control, SD-1, and SD-3 SnO_2 on quartz excited from e) perovskite side and f) quartz side. $\lambda_{ex} = 660$ nm.

(1.79-fold) (Figure S12, Supporting Information). The improved PL properties are more manifest in the time-resolved photoluminescence (TRPL) decays excited from the top perovskite layer, as shown in Figure 4c. Alike steady-state PL signals, the average lifetime (τ_{ave}) of TRPL was monotonically improved from 818.1 ns for the control to 868.7 and 897.5 ns for SD-1 and SD-3, respectively (Table S4, Supporting Information, the fitting curves are shown in Figure S13, Supporting Information). A longer lifetime is attributed to less nonradiative decays in the perovskite layers. In contrast, the τ_{ave} measured from the bottom SnO_2 side of the sample shows a drastic decrease with a sudden drop from 87.6 ns for the control to 66.8 and 46.1 ns for SD-1 and SD-3, respectively (Figure 4d and Table S4, Supporting Information). Since the charge carriers are generated at the position close to SnO_2 layer in this case, a shorter lifetime is readily explained by an efficient electron transfer from

perovskite absorber to SnO_2. Similarly to TRPL under the perovskite side excitation, TRMC decays show increased τ_{ave} from 604 ns for the control to 819 and 1040 ns for SD-1 and SD-3, respectively (Figure 4e and Table S5, Supporting Information). The TRMC results are in agreement with PL and TRPL measurements, supporting less trap-assisted nonradiative decay in the perovskite layers on sequentially deposited SnO_2 than that of control SnO_2. In contrast to TRPL results, TRMC decays excited from the SnO_2 side exhibit slightly decreased τ_{ave} but almost the same results with the perovskite-side excitation (Figure 4f). Being different from PL, TRMC probes mobile charge carriers surviving in the perovskite layer that are holes in the present case, because electrons are immediately extracted by the SnO_2 beneath. The fact that $\varphi\Sigma\mu_{max}$ values are mostly identical ($\approx 2.2 \times 10^{-5}\ m^2\ V^{-1}\ s^{-1}$) regardless of the SnO_2 type and the side of excitation suggests the hole mobilities are similar, while their decays are influenced by the quality of SnO_2. In other words, efficient electron transfer to sequentially deposited SnO_2 retard the nonradiative decays, which leads to long-lived holes. This is consistent with the results of electrochemical impedance spectroscopy (EIS) shown in Figure S14, Supporting Information. The Nyquist plots exhibited a single semicircle in the low-frequency region, indicative of the interfacial recombination resistance (R_{rec}) between the SnO_2 layer and the perovskite layer. Based on the fitting results using the equivalent circuit model (inset of Figure S14, Supporting Information), the R_{rec} value increased from 14.7 kΩ for the control sample to 17.4 and 16.2 kΩ for sequentially deposited SD-1 and SD-3, respectively. This higher R_{rec} suggests a decreased rate of charge recombination, which helps enhance V_{OC}.

Figure 5a shows the current density–voltage (JV) curves of the PSCs based on different SnO_2 as ETL. The champion PSC based on the control SnO_2 exhibits PCE = 20.48% with V_{OC}, fill factor (FF), and current density (J_{SC}) being 1.057 V, 0.771, and 25.11 mA cm^{-2}, respectively (**Table 2**). The statistics of the device are provided in Figure S15, Supporting Information. Notably, the champion PSC based on sequentially deposited SnO_2 (SD-1) delivers PCE = 21.75% with V_{OC}, FF, and J_{SC} being 1.062 V, 0.785, and 26.09 mA cm^{-2}, respectively. The PCE continues to increase for the 4-layered SnO_2 (SD-3) with PCE = 22.99% with V_{OC}, FF, and J_{SC} being 1.106 V, 0.795, and 26.13 mA cm^{-2}, respectively. Moreover, the hysteresis index (HI) decreases from 0.29 for the control to 0.06 and 0.08 for SD-1 and SD-3, respectively. Overall, sequentially deposited SnO_2 layers provide gains in all parameters of PSCs with the biggest gains in V_{OC}.

The external quantum efficiency (EQE) spectra of PSCs are shown in Figure 5b. The PSCs based on the control, SD-1, and SD-3 SnO_2 as the ETL provide similar integrated current density values of 23.61, 23.89, and 23.93 mA cm^{-2}, respectively, while the shape of the spectra slightly differ between the control and SD. The later PSCs have a slight gain in the 450–650 nm compared to the former, which is consistent with the marginal

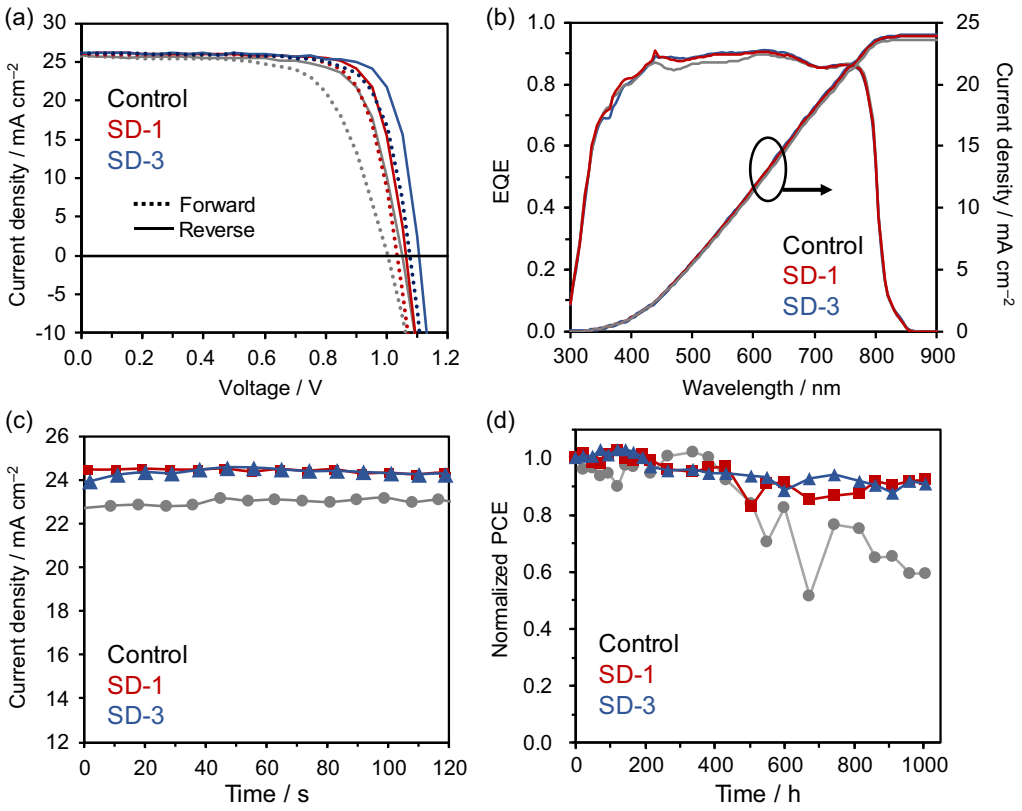

Figure 5. a) JV curves of the best PSC devices ($FAPbI_3$) prepared on control, SD-1, and SD-3 SnO_2. b) EQE spectra and integrated short circuit current density. c) Steady-state photocurrent measurements (PSCs based on control SnO_2 @0.876 V; SD-1 SnO_2 @0.865 V; SD-3 SnO_2 @0.891 V). d) Stability tests (up to ≈1.4 months) of PSCs stored at 20–25 °C, 30%–60% RH.

Table 2. Summary of PSC (FTO/SnO_2/$FAPbI_3$/HTL/Au) performance[a].

SnO_2	PCE [%]	J_{SC} [mA cm^{-2}]	V_{OC} [V]	FF	J_{SC}^{EQE} [mA cm^{-2}][b]	HI[c]
Control	20.48 (19.73 ± 0.57)	25.11 (25.36 ± 0.23)	1.057 (1.015 ± 0.042)	0.771 (0.767 ± 0.042)	23.61 (22.83 ± 0.74)	0.28 (0.16 ± 0.09)
SD-1	21.75 (21.09 ± 0.54)	26.09 (25.82 ± 0.23)	1.062 (1.056 ± 0.017)	0.785 (0.773 ± 0.014)	23.89 (23.78 ± 0.62)	0.06 (0.09 ± 0.06)
SD-3	22.99 (21.73 ± 0.42)	26.13 (26.13 ± 0.14)	1.106 (1.070 ± 0.019)	0.795 (0.770 ± 0.011)	23.93 (23.63 ± 0.53)	0.08 (0.10 ± 0.04)

[a]Under pseudo sunlight (100 mW cm^{-2}). The number of devices is more than 8 for each. The values are the maximum PCE and their device parameters in the reverse scan. The values in the brackets are the average and standard deviation. The HTL is doped spiro-OMeTAD. [b]Integrated J_{SC} from the EQE spectrum. [c]HI = (reverse PCE – forward PCE)/(reverse PCE).

increase in J_{SC} (sequentially deposited SnO_2 ETLs provide gain in $\Delta J_{SC} \approx 1$ mA cm^{-2}). This is linked to the more efficient electron extraction and transport for the sequentially deposited SnO_2, as evident from the TRPL and TRMC measurements. The steady-state (within 120 s) PCE of the PSCs with SD-1 and SD-3 SnO_2 were measured to be 21.83% (at 0.891 V) and 21.17% (at 0.865 V), respectively (Figure 5c), being larger than the steady-state PCE of 20.02 % (at 0.876 V) for the control SnO_2. As shown in Figure 5d, the PSCs without encapsulation remained at ≈90% of the initial PCE for the SD-1 and SD-3, while the control SnO_2 layer ensured only ≈60% of the initial PCE after 1000 h (≈1.4 month) of storage in the air. The decrease in PCE for the control device is due to the J_{SC} and V_{OC} (Figure S16, Supporting Information).

These results show that the device performance and stability embedded with sequentially deposited SnO_2 are significantly higher than those of the control 1 step-deposited SnO_2 device. The superior outputs of the former can be attributed to improved flatness and uniformity (decreased roughness and pinhole density) as well as increased surface free energies. These lead to improved electron transfer from perovskite to SnO_2 and reduced charge trapping in the active layer.

3. Conclusion

We introduced an SD method of SnO_2 as an ETL of PSCs that uses a diluted precursor suspension for subsequent depositions and achieves enhanced control over morphology and uniformity. This technique eliminates the need for additional chemicals and allows for a facile and quick preparation. From the DLS measurements, the dilution of SnO_2 suspension revealed a narrow distribution with a minimal particle size at less than 1:15 volume ratio. Notably, SD significantly decreased the average roughness of the SnO_2 layer (4.8 nm) and improved the flatness and coverage (reduced peak current in CV measurements). Interestingly, the SD yielded a thinner and more homogeneous SnO_2 layer (61.2 ± 8.8 nm) than the control (77.7 ± 26.3 nm), suggesting the removal of ill-formed agglomeration on the surface. The PSC based on a 4-layered sequentially deposited SnO_2 (SD-3) exhibited an improved maximum PCE of 22.99% with $V_{OC} = 1.106$ V, which was superior to the PCE of 20.48% with $V_{OC} = 1.057$ V of the control SnO_2 (conventional 1 step deposition from 1:3 diluted suspension). The observed enhancement was attributed to efficient electron transfer to SnO_2 and reduced charge trapping as evaluated from PL, TRPL, EIS, and TRMC. The facile and effective SD of SnO_2 would open up a versatile route toward low-temperature processed PSC with high performance, stability, and reproducibility.

4. Experimental Section

Materials and PSC Fabrication: Organic–inorganic perovskite solar cells based on $FAPbI_3$ were prepared as follows. FTO samples (8 Ω sq^{-1}) (Sigma-Aldrich) were etched using HCl and Zn to create a pattern to prevent shunting. Then, a compact SnO_2 layer was spin-coated on the substrates from SnO_2 aqueous colloidal dispersion (15 wt% in H_2O, Thermo Fisher Scientific Incorporation) diluted with deionized (DI) water to 1:3 (v:v), which was a conventional, control SnO_2. For the SD, the precursor was fatherly diluted according to Table 1. The dispersion was spin-coated at a certain rpm for 30 s. Then, the films were annealed on a hot plate at 120° C for 30 min. All the SnO_2 layers were passivated with Lithium carbonate by spin-coating of 20 mM Li_2CO_3[49] (99%, Wako Chemical Corp., WAKO) aqueous solution at 3000 rpm for 30 s followed by annealing at 100 °C for 15 min.

The deposition of the perovskite absorber was done in a nitrogen-filled glove box. The perovskite precursor solution contained 455 mg (0.72 mmol) of $FAPbI_3$ powder and 14 mg (0.24 mmol) of MACl (MA: methylammonium; >99.99%, Greatcell Solar), in 400 µL of a solvent consisting of *N*,*N*-dimethylformamide (DMF, super dehydrated, WAKO) and dimethyl sulfoxide (DMSO) (super dehydrated, WAKO) at DMF: DMSO = 4:1 in volume percentage (1.8 M). $FAPbI_3$ powder was prepared according to the reported procedure.[50] To deposit perovskite film, 65 µL of the precursor was spin-coated at 4000 rpm for 40 s; after 12 s of spinning, 200 µL of ethyl acetate (anhydrous, 99.8%, WAKO) was dispensed onto the rotating sample from a distance of 5–6 cm from the sample. Then the sample was annealed at 150 °C for 10 min outside ($T = 20$–25 °C; relative humidity (RH) = 20%–30%). Additionally, samples were annealed in a low vacuum of 60 kPa at 100 °C for 1 h to remove residual MACl.[51] Then, 16 mM of benzamidine hydrochloride (>97.0%, Tokyo Chemical Inc., TCI) in a mixed solvent of 2-propanol (WAKO, anhydrous, >99.5%) (IPA) and toluene (anhydrous, 99.8%, WAKO) (1:1, v:v) was spin-coated on the perovskite film followed by the annealing at 100 °C for 5 min outside. This passivation process was based on the previous report.[52] Next, a 50 µL of hole-transport layer (HTL) solution containing 60 mM spiro-OMeTAD (TCI, >98.0%), 30 mM 4-*tert*-butylpyridine (TBP, Sigma-Aldrich, 98%), and 37 mM lithium bis(trifluoromethanesulfonyl)imide (TCI, >98.0%) (dissolved in IPA) was spin-coated on perovskite layers at 4500 rpm for 30 s after filtering with 0.22 micron pore size syringe filter. Finally, gold electrodes with ≈70 nm thick were thermally evaporated on the samples with the evaporation rate not exceeding 1 Å s^{-1}.

General Measurements: Powder XRD measurements were conducted using a Rigaku MiniFlex-600 instrument equipped with Cu K_α radiation ($\lambda = 1.54$ Å). TRPL spectroscopy data were recorded using a HORIBA FluoroCube 3000U-UltraFast-SP spectrophotometer ($\lambda_{ex} = 377$ nm, resolution <50 ps). Steady-state UV–vis photoabsorption and PL spectroscopies were conducted using Jasco V-730 and Jasco FP-8300 spectrophotometers, respectively. Contact angle (θ) was measured using an Asumi Giken CAME1, and surface free energies were calculated by Kaelble–Uy theory: $\gamma_L(1 + \cos\theta) = 2(\gamma_S^d\gamma_L^d)^{1/2} + 2(\gamma_S^p\gamma_L^p)^{1/2}$, where γ_L and γ_S are SFEs of liquid and solid, respectively (d and p represent dispersion and polar components, respectively).[45] Cyclic voltammetry (CV) was performed with a potentiostat Gamry Interface 1010B at a scan rate of 10 mV s^{-1}. The electrochemical arrangement was three electrodes submerged in a 0.45 M KCl (>99.5%, Fluka) solution containing 5.5 mM $K_4Fe(CN)_6$ (>98.5%, Sigma Aldrich) and 4.5 mM $K_3Fe(CN)_6$ (>99%, Sigma Aldrich). The reference electrode was an Ag/AgCl electrode, and the counter electrode was platinum. DLS to measure particle size distribution in water (refractive index: 1.33, viscosity: 0.8872 mPa s^{-1}) was performed by using a Malvern ZetasizerLab. SEM/EDX was performed on a field emission SEM JEOL JSM-IT700HR with am EDX JEOL JED-2300 at 5 and 10 keV, respectively. The grain size of perovskite was evaluated using MorphoLibJ library in ImageJ. AFM measurements were performed using a Bruker Innova AFM in tapping mode, operating at a scan rate of 1 Hz with a resolution of 512 scan lines per image. Current density–voltage curves were measured using a source meter unit (SMU) (ADCMT Corp., 6241 A) under AM 1.5 G pseudo solar illumination at 100 mW cm^{-2} from a 300 W solar simulator (SAN-EI, XES-301S, monitored by a calibrated standard cell of Bunko Keiki BS-520BK). The active area through a mask was 0.085 cm^2. The scan was conducted from 1.2 to 0 V and then backward, with a step size of 0.05 V and a hold time of 100 ms. EQE spectra were recorded using a Bunko Keiki model SM-250KD equipped with a Keithley model 2401 SMU. The monochromated light power of the EQE instrument was calibrated using a silicon photovoltaic cell (Bunko Keiki model S1337-1010BQ). XPS analyses were conducted using a KRATOS ULTRA2 photoelectron analyzer under a base pressure of $\approx 10^{-7}$ Pa. The instrument utilized Al K_α radiation ($h\nu$ = 1486.6 eV) at an operational power of 300 W (15 kV, 20 mA). The impedance and phase-angle shift were measured using an impedance analyzer Hioki IM3570. The data were measured at 1.0 V in the frequency range of 1 MHz to 4 Hz in the dark. All the measurements were performed at 25 °C in the air.

TRMC: Perovskite and ETL were prepared in the same manner as the solar cells on a quartz plate. The sample was placed within a resonant cavity and subjected to continuous microwaves at ≈9.1 GHz. The excitation laser utilized for measuring perovskite, sourced from an optical parametric oscillator (OPO, Continuum, Inc., Panther) and seeded by the second harmonic generation (355 nm) of a Nd:YAG laser (Continuum, Inc., Surelite II, with a pulse duration of 5–8 ns at 10 Hz), was set to 660 nm. For measuring SnO_2, the excitation laser was generated by the fourth harmonic generation (266 nm) of the same laser system. The photoconductivity transient, $\Delta\sigma$, was transformed into the product of the quantum efficiency (φ) and the combined charge carrier mobilities, $\Sigma\mu$ (= $\mu_h + \mu_e$) by $\varphi\Sigma\mu = \Delta\sigma\,(eI_0F_{light})^{-1}$, where e and F_{light} are the unit charge of a single electron and a correction (or filling) factor, respectively. The measurements were performed at 25 °C in the air.

Supporting Information

Supporting Information is available from the Wiley Online Library or from the author.

Acknowledgements

The authors acknowledge the financial support received from the New Energy and Industrial Technology Development Organization (NEDO) Green Innovation Project (JP21578854 to A.W. and A.S.), KAKENHI of the Japan Society for the Promotion of Science (JSPS) (JP20H05836 and JP24H00484 to A.S.), the Japan Science and Technology Agency (JST) CREST (JPMJCR23O2 to A.S.) and MIRAI (JPMJMI22E2 to A.W. and A.S.), and International Collaborative Research Program of ICR, Kyoto University (Project No. 2024-43 to A.W. and A.S.). We thank Shaoxian Li at Osaka University for his assistance in TRMC measurements.

Conflict of Interest

The authors declare no conflict of interest.

Data Availability Statement

The data that support the findings of this study are available in the supplementary material of this article.

Keywords

diluted dispersion, electron transport layers, lead halide perovskite solar cells, SnO_2

Received: June 3, 2024
Revised: June 25, 2024
Published online: July 12, 2024

[1] W. Chen, Y. Wu, Y. Yue, J. Liu, W. Zhang, X. Yang, H. Chen, E. Bi, I. Ashraful, M. Grätzel, L. Han, *Science* **2015**, *350*, 944.
[2] A. Kojima, K. Teshima, Y. Shirai, T. Miyasaka, *J. Am. Chem. Soc.* **2009**, *131*, 6050.
[3] H. Min, D. Y. Lee, J. Kim, G. Kim, K. S. Lee, J. Kim, M. J. Paik, Y. K. Kim, K. S. Kim, M. G. Kim, T. J. Shin, S. Il Seok, *Nature* **2021**, *598*, 444.
[4] S. D. Stranks, G. E. Eperon, G. Grancini, C. Menelaou, M. J. P. Alcocer, T. Leijtens, L. M. Herz, A. Petrozza, H. J. Snaith, *Science* **2013**, *342*, 341.
[5] J. Xu, A. Buin, A. H. Ip, W. Li, O. Voznyy, R. Comin, M. Yuan, S. Jeon, Z. Ning, J. J. McDowell, P. Kanjanaboos, J.-P. Sun, X. Lan, L. N. Quan, D. H. Kim, I. G. Hill, P. Maksymovych, E. H. Sargent, *Nat. Commun.* **2015**, *6*, 7081.
[6] W. S. Yang, J. H. Noh, N. J. Jeon, Y. C. Kim, S. Ryu, J. Seo, S. Il Seok, *Science* **2015**, *348*, 1234.
[7] Y. Dong, J. Duan, D. Luo, J. Liu, X. Wang, X. Liu, Z. Huang, X. Li, Y. Gao, *Mater. Today Commun.* **2024**, *39*, 108695.
[8] X. Feng, B. Liu, M. Cai, J. Yang, *J. Mater. Chem. C* **2023**, *11*, 11295.
[9] Y. Wang, M. Feng, H. Chen, M. Ren, H. Wang, Y. Miao, Y. Chen, Y. Zhao, *Adv. Mater.* **2024**, *36*, 2305849.
[10] Z. Wu, J. Su, N. Chai, S. Cheng, X. Wang, Z. Zhang, X. Liu, H. Zhong, J. Yang, Z. Wang, J. Liu, X. Li, H. Lin, *Adv. Sci.* **2023**, *10*, 2300010.
[11] N. Kumar, H. B. Lee, B. Tyagi, M. M. Ovhal, S. Cho, J. S. Lee, J. W. Oh, J. W. Kang, *Sol. RRL* **2023**, *7*, 2300065.
[12] P. Panneerselvam, S. Ramasamy, S. P. Rajendra, M. S. AlSalhi, J. Guo, S. Angaiah, *Adv. Mater. Technol.* **2023**, *8*, 2201551.
[13] X. Liu, Q. Hu, Y. Peng, X. Peng, W. Zhao, H. Li, H. Wang, X. Zhang, Y. Lei, *J. Phys. Chem. Lett.* **2023**, *14*, 9433.
[14] J. Wang, Z. Dong, J. Wang, J. Zhang, Z. Zhai, F. Qiu, J. Wu, Y. Lin, J. Zhang, *J. Mater. Chem. A* **2023**, *11*, 22206.
[15] M. Nukunudompanich, K. Suzuki, K. Kameda, S. Manzhos, M. Ihara, *RSC Adv.* **2023**, *13*, 27686.

[16] Y. Ren, B. Li, Y. Zhu, Z. Zhang, Q. Luo, H. Weng, X. Tan, P. Xiang, X. Tan, *Sol. RRL* **2023**, *7*, 2300554.
[17] J. Park, J. Kim, H.-S. Yun, M. J. Paik, E. Noh, H. J. Mun, M. G. Kim, T. J. Shin, S. Il Seok, *Nature* **2023**, *616*, 724.
[18] X. Zhang, Y. Zhou, M. Chen, D. Wang, L. Chao, Y. Lv, H. Zhang, Y. Xia, M. Li, Z. Hu, Y. Chen, *Small* **2023**, *19*, 2303254.
[19] T. Yan, C. Zhang, S. Li, Y. Wu, Q. Sun, Y. Cui, Y. Hao, *Adv. Funct. Mater.* **2023**, *33*, 2302336.
[20] S. Zhang, X. Jia, Q. Geng, Z. He, Y. Hu, Y. Gao, S. Yang, C. Yao, Q. Zhang, D. Wang, Y. Wu, *Surf. Interfaces* **2023**, *41*, 103226.
[21] J. Gong, Y. Cui, F. Li, M. Liu, *Small Sci.* **2023**, *3*, 2200108.
[22] A. Pramitha, S. G. Rao, Y. Raviprakash, *J. Electron. Mater.* **2023**, *52*, 8124.
[23] P. Senthilkumar, S. Raja, R. Ramesh Babu, V. Kavinkumar, K. Jothivenkatachalam, G. Vasuki, *Appl. Phys. A* **2023**, *129*, 675.
[24] J. Tao, X. Liu, J. Shen, H. Wang, J. Xue, C. Su, H. Guo, G. Fu, W. Kong, S. Yang, *Chem. Eng. J.* **2022**, *430*, 132683.
[25] R. Wang, J. Wu, S. Wei, J. Zhu, M. Guo, Q. Zheng, M. Wei, S. Cheng, *J. Power Sources* **2022**, *544*, 231870.
[26] S. Kim, F. Zhang, J. Tong, X. Chen, E. Enkhbayar, K. Zhu, J. Kim, *Sol. Energy* **2022**, *233*, 353.
[27] X. Huang, J. Du, X. Guo, Z. Lin, J. Ma, J. Su, L. Feng, C. Zhang, J. Zhang, J. Chang, Y. Hao, *Sol. RRL* **2020**, *4*, 1900336.
[28] Y. Mo, C. Wang, X. Zheng, P. Zhou, J. Li, X. Yu, K. Yang, X. Deng, H. Park, F. Huang, Y. Cheng, *Interdiscip. Mater.* **2022**, *1*, 309.
[29] T. Luo, G. Ye, X. Chen, H. Wu, W. Zhang, H. Chang, *ACS Appl. Mater. Interfaces* **2022**, *14*, 42093.
[30] D. Bai, D. Zheng, S. Yang, L. Peng, P. Wang, J. Liu, X. Zhu, D. Yang, S. F. Liu, *Sol. RRL* **2024**, *8*, 2301036.
[31] Z. Su, D. Xu, Q. Ma, K. Gao, C. Zhang, C. Xing, S. Wang, W. Shi, X. Wang, K. Li, J. Hui, X. Yang, *Sol. RRL* **2023**, *7*, 2201026.
[32] H. J. Lee, J. K. Park, J. H. Heo, S. H. Im, *Energy Environ. Mater.* **2024**, *7*, e12582.
[33] J. Xia, M. Sohail, M. K. Nazeeruddin, *Adv. Mater.* **2023**, *35*, e2211324.
[34] L. Han, H. Hu, M. Yuan, P. Lin, P. Wang, L. Xu, X. Yu, C. Cui, *Nanotechnology* **2023**, *34*, 305401.
[35] C. Deng, X. Liu, Z. Huang, K. Chen, H. Ren, M. Xu, Z. Zhang, K. Hu, C. Yang, H. Yu, *Sol. RRL* **2023**, *7*, 21269.
[36] N. Sarda, A. Vidhan, S. Basak, P. Hazra, T. Behera, S. Ghosh, R. J. Choudhary, A. Chowdhury, S. K. Sarkar, *ACS Appl. Energy Mater.* **2023**, *6*, 3996.
[37] X. Ling, J. Guo, C. Shen, Y. Li, H. Tian, X. Yuan, L. Gui, X. Zhang, B. Li, S. Chen, R. Li, J. Yuan, W. Ma, Y. Deng, *Small* **2024**, *20*, 2308579.
[38] K. Zhang, X. Tan, P. Xiang, B. Li, J. Li, Y. Ren, Y. Zhu, Y. Liu, W. Yan, X. Chen, H. Han, *J. Alloys Compd.* **2023**, *946*, 169361.
[39] L. Zhang, C. Fu, S. Wang, M. Wang, R. Wang, S. Xiang, Z. Wang, J. Liu, H. Ma, Y. Wang, Y. Yan, M. Chen, L. Shi, Q. Dong, J. Bian, Y. Shi, *Adv. Funct. Mater.* **2023**, *33*, 2213961.
[40] Y. Zhao, R. Ge, J. Zheng, L. Chen, X. Wang, Y. Zheng, L. Zhong, Y. Zhu, X. Xu, G. Xu, X. Xiao, *Energy Technol.* **2023**, *11*, 2300611.
[41] Y. Wang, Q. Ye, P. Hang, Y. Yao, B. Li, C. Kan, D. Zhang, X. Yu, D. Yang, *J. Mater. Sci.* **2023**, *58*, 14807.
[42] D. Beynon, E. Parvazian, K. Hooper, J. McGettrick, R. Patidar, T. Dunlop, Z. Wei, P. Davies, R. Garcia-Rodriguez, M. Carnie, M. Davies, T. Watson, *Adv. Mater.* **2023**, *35*, 2208561
[43] K. Park, S. Tan, T. Kodalle, D. Lee, M. Abdelsamie, J. Park, J. Lee, S. Jung, J. H. Ko, N. Park, C. M. Sutter-Fella, Y. Yang, J. Lee, *Adv. Mater.* **2024**, *36*, 2307265.
[44] P. Wang, Z. Shao, M. Ulfa, T. Pauporté, *J. Phys. Chem. C* **2017**, *121*, 9131.
[45] D. H. Kaelble, *J. Adhes.* **1970**, *2*, 66.
[46] D. Flak, Q. Chen, B. S. Mun, Z. Liu, M. Rękas, A. Braun, *Appl. Surf. Sci.* **2018**, *455*, 1019.
[47] S. Kumar, R. B. Choudhary, *J. Mol. Struct.* **2023**, *1293*, 136199.
[48] A. Saeki, *Polym. J.* **2020**, *52*, 1307.
[49] Y. Zhang, T. Kong, H. Xie, J. Song, Y. Li, Y. Ai, Y. Han, D. Bi, *ACS Energy Lett.* **2022**, *7*, 929.
[50] Y. Zhang, S. Seo, S. Y. Lim, Y. Kim, S.-G. Kim, D.-K. Lee, S.-H. Lee, H. Shin, H. Cheong, N.-G. Park, *ACS Energy Lett.* **2020**, *5*, 360.
[51] D.-H. Kang, S.-U. Lee, N.-G. Park, *ACS Energy Lett.* **2023**, *8*, 2122.
[52] F. Ye, T. Tian, J. Su, R. Jiang, J. Li, C. Jin, J. Tong, S. Bai, F. Huang, P. Müller-Buschbaum, Y. Cheng, T. Bu, *Adv. Energy Mater.* **2024**, *13*, 2302775.